Biochemistry

pubs.acs.org/biochemistry Article

Pan-3C Protease Inhibitor Rupintrivir Binds SARS-CoV-2 Main Protease in a Unique Binding Mode

Gordon J. Lockbaum, Mina Henes, Jeong Min Lee, Jennifer Timm, Ellen A. Nalivaika, Paul R. Thompson, Nese Kurt Yilmaz, and Celia A. Schiffer*

Cite This: https://doi.org/10.1021/acs.biochem.1c00414 Read Online

ACCESS | Metrics & More | Article Recommendations | Supporting Information

ABSTRACT: Rupintrivir targets the 3C cysteine proteases of the picornaviridae family, which includes rhinoviruses and enteroviruses that cause a range of human diseases. Despite being a pan-3C protease inhibitor, rupintrivir activity is extremely weak against the homologous 3C-like protease of SARS-CoV-2. In this study, the crystal structures of rupintrivir were determined bound to enterovirus 68 (EV68) 3C protease and the 3C-like main protease (M^{pro}) from SARS-CoV-2. While the EV68 3C protease–rupintrivir structure was similar to previously determined complexes with other picornavirus 3C proteases, rupintrivir bound in a unique conformation to the active site of SARS-CoV-2 M^{pro} splitting the catalytic cysteine and histidine residues. This bifurcation of the catalytic dyad may provide a novel approach for inhibiting cysteine proteases.

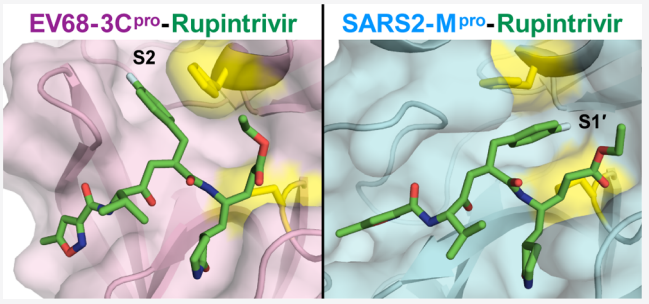

There are over 200 viral species that are known to infect humans, with three to four new human viral pathogens discovered every year.[1] Viral outbreaks result in the death of hundreds to millions of people, as in the case of the coronavirus infectious disease 2019 (COVID-19) pandemic caused by SARS-CoV-2. Many of the most common human viral pathogens are from the picornaviridae family. This viral family includes rhinoviruses that cause common cold and enteroviruses associated with several diseases ranging from hand-foot-and-mouth disease to polio-like neuropathies. For example, the enterovirus EV68 has been linked to acute flaccid myelitis (AFM), affecting the gray matter of the spinal cord, leading to polio-like neurological symptoms such as muscle weakness. Between August 2014 and January 2020, an EV68 outbreak caused over 600 confirmed cases of AFM across 34 states.[2] Unfortunately, many of the diseases caused by these viruses lack effective treatment options.

In the absence of vaccines or natural antibodies, direct acting antivirals (DAAs) are a critical therapeutic strategy to suppress viral outbreaks and treat the most vulnerable in the population. DAAs save millions of lives every year by targeting essential viral enzymes to prevent viral replication. Viral proteases, which cleave polyproteins to allow viral maturation, are key therapeutic targets. Inhibition of viral proteases with small-molecule inhibitors has a proven therapeutic track record, as with HIV-1 and HCV,[3−6] some of which have been shown to have potency against SARS-CoV-2 proteases.[7−9] Rhinoviruses and enteroviruses have a 3C protease ($3C^{pro}$) that is necessary for viral maturation. The 3C proteases of various viral species are structurally very similar (Figure 1A). SARS-CoV-2 has two viral proteases, the papain-like protease (PL^{pro}) and the main protease (M^{pro}). M^{pro} is also known as the 3C-like protease because the active site domain is structurally similar to 3C proteases. SARS-CoV-2 M^{pro} is larger than the 3C proteases (306 AA vs ∼180 AA) due to additional residues near the active site (residues 43−62) and a 100-residue domain III (Figure 1B). The structural similarities especially in the active site suggest the potential of an effective cross-3C/3C-like protease inhibitor.

In an attempt to cure common cold, Pfizer developed rupintrivir (Figure 1C), an irreversible covalent inhibitor designed to target the 3C cysteine protease of human rhinovirus B.[10] Rupintrivir inhibits several rhinovirus serotypes and patient isolates with an EC50 between 3 and 183 nM.[11] In 2003, a phase 2 randomized, double-blind, placebo-controlled study showed that rupintrivir caused significant prophylaxis and daily symptom reduction[12] and had good safety and pharmacokinetics in healthy volunteers.[13] Rupintrivir was later shown to potently inhibit the 3C proteases of several enterovirus strains with a low-nanomolar EC50[11,14,15] with a similar binding mode (Figure 1A). Despite their similarities, rupintrivir only weakly inhibits the M^{pro} of SARS-CoV-1 and 2

Received: June 17, 2021

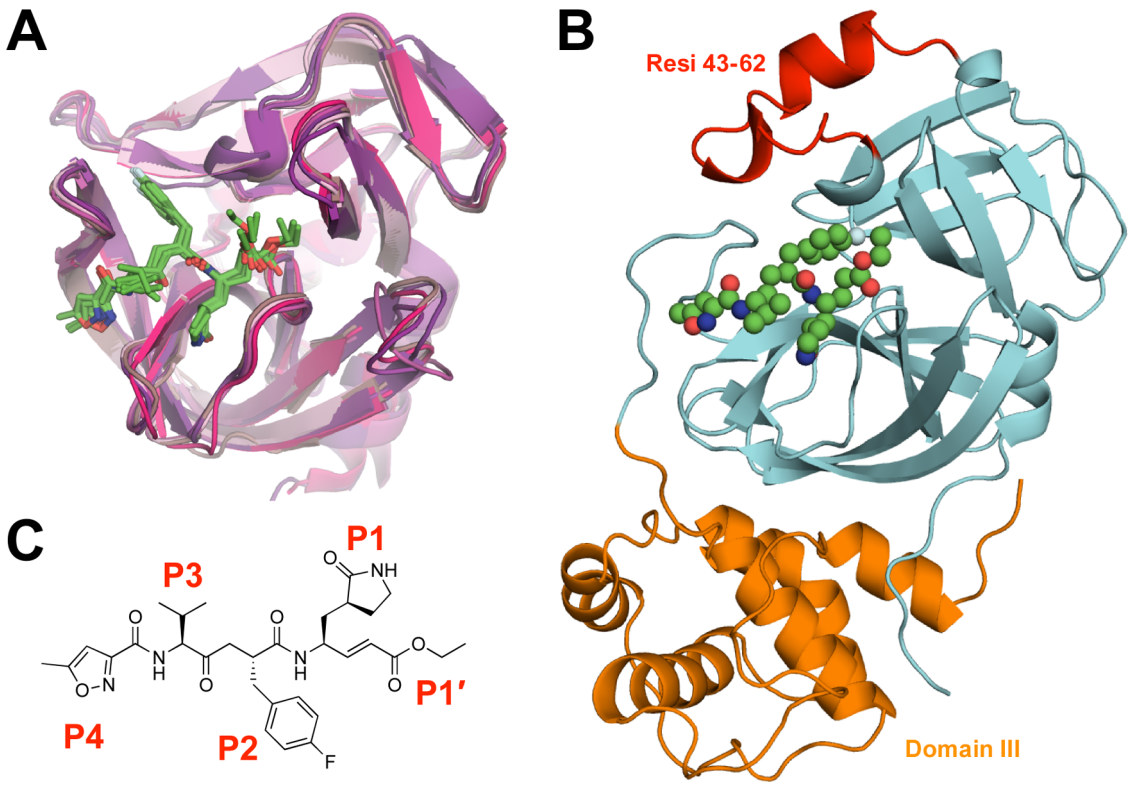

Figure 1. (A) Rupintrivir in complex with viral 3C proteases of rhinovirus A, rhinovirus C, coxsackievirus, enterovirus 71, enterovirus 93, and novel enterovirus 68. The crystal structures are superimposed in cartoon representation with rupintrivir shown as green sticks (PDB: 1CQQ, 3RUO, 3SJI, 3SJO, 6KU8, 7L8H). (B) Novel SARS-CoV-2 M^{pro}-rupintrivir crystal structure in cartoon representation with rupintrivir shown as spheres, protease residues 43−62 colored red, the domain that is structurally homologous to 3C proteases colored cyan, and domain III colored orange (PDB: 7L8I). (C) Chemical structure of rupintrivir.

with IC_{50} values of >100 μM and 68 ± 7 μM, respectively.[16,17] However, the binding mode of rupintrivir underlying this potency loss was not clear as the structure of SARS-CoV-2 M^{pro} in complex with rupintrivir had not been determined.

In this study, we present the crystal structures of both EV68 $3C^{pro}$ and SARS-CoV-2 M^{pro} with rupintrivir bound at the active site. EV68 $3C^{pro}$ binds rupintrivir in the previously observed canonical binding mode; however, in the SARS-CoV-2 M^{pro} complex, rupintrivir adopts a unique binding mode. The SARS-CoV-2 M^{pro}−rupintrivir complex structure reveals how both the inhibitor and the protease active site undergo conformational changes to accommodate rupintrivir by bifurcating the catalytic dyad.

To elucidate the structure and binding mode of rupintrivir in inhibiting coronaviral M^{pro}, the crystal structure of rupintrivir in complex with SARS-CoV-2 M^{pro} was determined. We also determined the crystal structure of rupintrivir bound to enteroviral EV68 $3C^{pro}$ for comparison. The inhibitor binding modes and catalytic dyad side-chain conformations were validated by composite omit maps with and without simulated annealing (Figure S1). Additional details regarding diffraction data and inhibitor modeling are provided in the Materials and Methods section and Table S2.

The EV68 $3C^{pro}$−rupintrivir complex structure was determined at 1.95 Å resolution (R_{factor}/R_{free} = 15.8/18.6%) in the space group R3 with two molecules in the asymmetric unit (AU). As expected, rupintrivir's binding conformation in EV68 $3C^{pro}$ active site is identical to all other previously published 3C proteases, with the P2 fluorophenylalanine located in the S2 subsite (Figure 2A). Unlike some of the other $3C^{pro}$−rupintrivir complexes,[18] our structure has the catalytic histidine (His40) in only one conformation. The P2 fluorophenylalanine fits in the hydrophobic channel (Figure 2B), and the fluorine participates in a halogen-bonding interaction with Thr129 while pi-stacking with the catalytic His40 (Figure 2C). Other hydrogen bonds between the inhibitor and protease include several interactions to the backbone atoms of Gly164 and Asn165, which likely interact with the cleavage sites (Figure 2D).

The SARS-CoV-2 M^{pro}−rupintrivir complex structure was determined in two different space groups. The structure in the $P2_1$ space group had a 2.10 Å resolution (R_{factor}/R_{free} = 20.6/26.3%) with two monomers in the AU while the structure in the $P2_12_12$ space group was determined at 2.45 Å resolution (R_{factor}/R_{free} = 22.4/28.1%) with a single molecule in the AU. Contrary to all previous rupintrivir structures with 3C proteases, in complex with SARS-CoV-2 M^{pro}, the P2 fluorophenylalanine moiety is intercalated between the catalytic residues (His41 and Cys145 in M^{pro}) pointing toward the S1' subsite (Figure 2E,F) instead of binding in the S2 subsite. This was true for both monomers in the structure solved in the $P2_1$ space group, as well as in the structure solved in the $P2_12_12$ space group, both of which were validated by omit maps (Figure S1). Thus, this unique conformation is present in all three complex structures determined. In this binding mode, rather than occupying the S2 subsite, the P2 fluorophenylalanine splits the catalytic active site, stacking against His41 (Figure 2F,G).

A major distinction in the binding mode of rupintrivir in the active site of M^{pro} is the conformation of the fluorophenyla-

https://doi.org/10.1021/acs.biochem.1c00414
Biochemistry XXXX, XXX, XXX−XXX

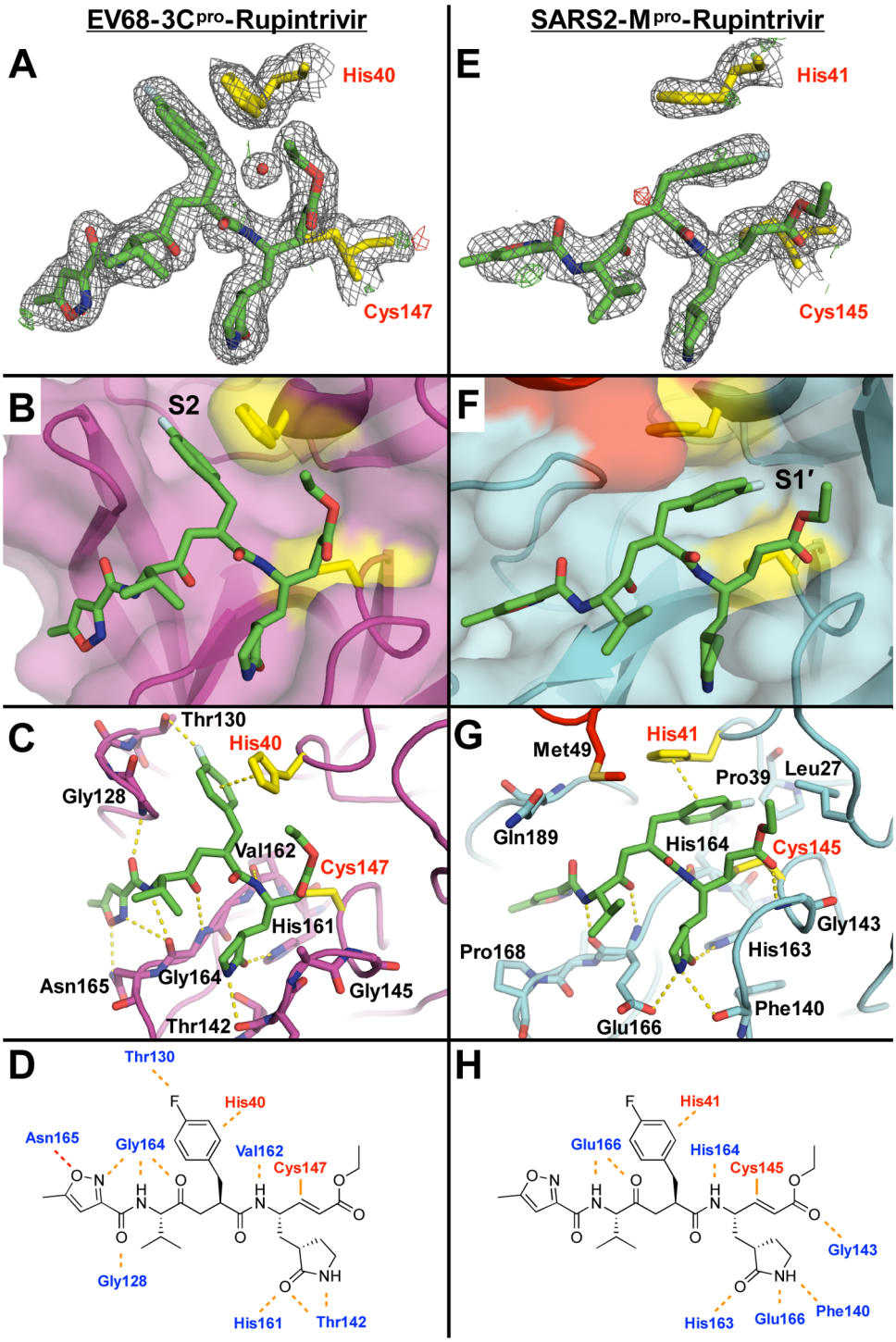

Figure 2. (A, E) Rupintrivir and catalytic residues in the crystal structures of enterovirus 68 3C protease (EV68 3C^{pro}) and SARS-CoV-2 M^{pro} (SARS2-M^{pro}), shown within the electron density. The $2F_o - F_c$ direct maps are depicted as gray mesh contoured at 1.0 σ, while the $F_o - F_c$ difference maps have positive density depicted as green mesh contoured at 3.0σ and negative density as red mesh contoured at −3.0 σ. (B, F) Binding mode of rupintrivir at the active site of proteases in the crystal structures. Rupintrivir shown as sticks and protease active site shown as cartoon with transparent surface. (C, G) Residues involved in hydrogen bonding with rupintrivir are shown as sticks. (D, H) Intermolecular hydrogen bonds between rupintrivir and protease in EV68 3C^{pro} and SARS-CoV-2 M^{pro} crystal structures. PDB: 7L8H (left) and 7L8I (right).

lanine, which normally occupies the S2 subsite when bound to 3C proteases. While the majority of the SARS-CoV-2 M^{pro} substrates have leucine as the P2 residue, the S2 subsite also accommodates phenylalanine and valine.[19] However, with the fluorophenylalanine, which introduces polarity, the interactions become unfavorable in the hydrophobic S2 subsite. In SARS-CoV-2 M^{pro}, there is a lack of space to create polar interactions while optimally maintaining the other backbone hydrogen bonds (Figure S2), despite some polar atoms such as the side-chain hydroxyl of Tyr54 in the back of the S2 pocket. Instead, the P2 fluorophenylalanine is oriented toward the S1' pocket, bifurcating the two catalytic residues. In this unique binding

https://doi.org/10.1021/acs.biochem.1c00414
Biochemistry XXXX, XXX, XXX−XXX

mode, the P2 ring makes pi-stacking interactions with the catalytic histidine, but the fluorine atom does not have any polar interactions in the S1' pocket (Figure 2G). This alternative orientation of the P2 group and lack of specific fluorine interactions likely contribute to rupintrivir's reduced potency against SARS-CoV-2 M^{pro}.

In addition to those of the P2 moiety, other interactions of rupintrivir are also compromised when bound to SARS-CoV-2 M^{pro} compared with the EV68 $3C^{pro}$−rupintrivir complex. When bound to EV68 $3C^{pro}$, rupintrivir forms a network of five hydrogen bonds through the P3−P4 moieties with the protease active site, while with SARS-CoV-2 M^{pro}, only two are formed. In particular, the hydrogen bond formed in the EV68 $3C^{pro}$ complex with the backbone nitrogen of Gly128 is missing in M^{pro} as the two enzymes are distinct around that region of the protease fold (Figure 2C,D vs G,H). These losses in specific hydrogen bonding may also contribute to the dramatic loss in rupintrivir potency.

Rupintrivir is a potent antiviral protease inhibitor that successfully targets a whole family of picornaviridae $3C^{pro}$ enzymes, promising that a pan-viral DAA is not out of reach. In this study, we determined the crystal structure of the EV68 $3C^{pro}$−rupintrivir complex and demonstrated that rupintrivir binds in the canonical mode for piconaviral $3C^{pro}$ complexes. The SARS-CoV-2 M^{pro} is a 3C-like protease with a homologous domain harboring a similar active site, but rupintrivir is not a potent M^{pro} inhibitor.[17] The molecular basis for the lack of potency was revealed by determining the structure of the SARS-CoV-2 M^{pro}−rupintrivir complex here, which shows a loss of hydrogen-bonding network throughout the active site as well as a unique binding mode involving repositioning of the P2 fluorophenylalanine moiety. While this manuscript was under review, a crystal structure of the SARS-CoV-2 M^{pro}−rupintrivir complex (PDB-ID: 7P35[20]) was released, where the P2 moiety was accommodated at the S2 site with considerable rearrangement of both the protease and the inhibitor with overall weakened interactions (Figure S2), suggesting a dynamic equilibrium of P2 orientations. Orientation of the P2 group toward the S1' subsite in our structure presents opportunities to optimize interactions in this region and potentially grow the inhibitor toward the primed side of the active site. When bound to M^{pro}, rupintrivir's P2 group splits the catalytic active site of this cysteine protease, physically separating the catalytic dyad. This bifurcation orients the catalytic histidine side chain in a conformer distal from the cysteine. Previous structures have observed multiple conformers for the catalytic histidine in some of which water molecules were observed separating the catalytic residues (Figure S4). Additionally, recent computational work confirmed the mobility of the catalytic dyad.[21] This conformational plasticity is consistent with rupintrivir's binding mode observed in our structure, which can be further exploited in inhibitor design. To our knowledge, splitting a catalytic active site by an inhibitor has not previously been observed and may represent a new strategy for disrupting cysteine proteases in the design of pan-viral protease inhibitors.

MATERIALS AND METHODS

EV68 $3C^{pro}$ Expression and Purification. The gene encoding EV68 $3C^{pro}$ was subcloned in the IPTG-inducible pET28 expression vector. DNA (1 μL) was added to *Escherichia coli* BL21-DE3 cells and incubated on ice for 20 min. The cells were heat-shocked at 42 °C for 30 s, 200 μL of SOC media were added and the cells were grown at 37 °C for 1 h on a shaker. The entire 200 μL was then plated on an LB/Kan plate and grown overnight at 37 °C. The following morning, one colony was inoculated in 10 mL of LB in an Erlenmeyer flask and kanamycin was added to a final concentration of 35 μg/mL. The cells were grown at 37 °C for 10 h on a shaker. The entire 10 mL was then added to 285 mL of LB, kanamycin was added to a final concentration of 35 μg/mL, and the culture was grown at 37 °C overnight. The overnight culture was used to inoculate 6 L of TB media and cells were grown at 37 °C in the presence of kanamycin until an OD_{600} of 0.45, and then the temperature was decreased to 18 °C until an OD_{600} of 0.6, where the cells were induced with 250 mL of 1 mM IPTG. The cells grown overnight at 18 °C were harvested and frozen. The harvested cells were thawed at RT, resuspended in EV Ni1 buffer [50 mM HEPES pH 7.5, 300 mM NaCl, 10 mM Imidazole, and 2 mM DTT], and lysed with a cell disruptor. Cell debris was removed by centrifugation at 25 000 rcf at 4 °C for 1 h. A 1 mL HisTrap crude FF column was equilibrated in a 5× column volume of EV Ni1 buffer. The soluble lysate was loaded onto the HisTrap column and the flow-through was collected. The column was then washed with 100 mL of EV Ni1 buffer, and the wash was collected. The protein was eluted with 30 mL of EV Ni2 buffer [50 mM HEPES pH 7.5, 300 mM NaCl, 250 mM imidazole, and 2 mM DTT], and the elution was collected in the presence of 50 units of thrombin. The collected elution was dialyzed overnight against 2 L of EV SEC buffer [25 mM HEPES pH 7.5, 300 mM NaCl, and 2 mM DTT] at 4 °C. After dialysis, any precipitate was removed by centrifugation and the protein was concentrated to 1.25 mg/mL. For crystallography, an additional purification step was performed with a Pharmacia Superdex 75 16/60 FPLC column equilibrated in EV SEC buffer. EV68-$3C^{pro}$ fractions purified from the size exclusion column were concentrated to 0.92−6.2 mg/mL using an Amicon Ultra-15 10 kDa device (Millipore) for crystallization.

EV68 $3C^{pro}$-Rupintrivir Cocrystallization. Discovery of the condition producing cocrystals of EV68-3Cpro and rupintrivir without seeding was achieved using the PACT Premier Screen (Molecular Dimensions), in Well F4, consisting of 20% (w/v) PEG 3350, 0.1 M bis-tris propane pH 6.5, and 0.2 M potassium thiocyanate, with a protease concentration of 6.6 mg/mL and 10-fold molar excess of rupintrivir. Crystals from well F4 of the PACT Premier screen were used for microseeding. Cocrystals were grown at RT by the hanging drop vapor diffusion method in 24-well VDX handing-drop trays (Hampton Research) with protease concentrations of 0.92, 2.1, 3.76, and 6.2 mg/mL and 10-fold molar excess of rupintrivir. Crystallization drops were set with the reservoir solution consisting of 10−30% PEG 3350, 0.2 M potassium thiocyanate, and 0.1 M Bis-Tris propane pH 6.5 set with 2 μL of well solution and 1 μL of protein microseeded with a cat whisker. The condition that produced the best crystals for data collection was 15% (w/v) PEG 3350 with a protease concentration of 3.76 mg/mL and 10-fold molar excess of rupintrivir. Data were collected at 100 K using cryogenic conditions containing the precipitant solution supplemented with 25% glycerol.

SARS-CoV-2 M^{pro} Expression and Purification. SARS-CoV-2 M^{pro} was expressed and purified as previously described.[22] Briefly, the plasmid was transformed into *E. coli* strain HI-Control BL21(DE3) (Lucigen). The transformed cells were precultured at 37 °C in LB medium with ampicillin

https://doi.org/10.1021/acs.biochem.1c00414
Biochemistry XXXX, XXX, XXX−XXX

(100 μg/mL) overnight, and the cell culture was inoculated into TB medium containing 50 mM sodium phosphate (pH 7.0) and ampicillin (100 μg/mL). When the OD_{600} value reached ∼2.0, 0.5 mM IPTG was added to induce M^{pro} expression and the cell culture was further incubated overnight at 20 °C. The cells were harvested by centrifugation at 5000 rpm for 20 min, resuspended in lysis buffer (50 mM Tris−HCl (pH 8.0), 400 mM NaCl, 1 mM TCEP), and lysed by a cell disruptor. The lysate was clarified by ultracentrifugation at 18 000 rpm for 50 min. The supernatant was loaded onto a HisTrap FF column (GE Healthcare) equilibrated with lysis buffer, washed with lysis buffer, and followed by elution using an elution buffer (50 mM Tris−HCl pH 8.0, 400 mM NaCl, 500 mM imidazole, 1 mM TCEP) with a linear gradient of imidazole ranging from 0 to 500 mM. The fractions of M^{pro}-His tag were mixed with GST-PreScission protease-His-tag at a molar ratio of 5:1 to remove the C-terminal His tag. The PreScission-treated M^{pro} was applied to the nickel column to remove the GST-PreScission protease-His-tag and protein with uncleaved His-tag. The His-tag cleaved M^{pro} in the flow-through was further purified by size exclusion chromatography (HiLoad 16/60 Superdex 75, GE Healthcare) and stored in 20 mM HEPES pH 7.5, 150 mM NaCl, 1 mM TCEP.

SARS-CoV-2 M^{pro} Crystallization. SARS-CoV-2 M^{pro} cocrystallized in multiple conditions. One condition producing large platelike crystals was discovered using the MCSG-1 crystal screen (Anatrace), Well B2, containing 25% (w/v) PEG 3350 and 0.1 M bis-tris-methane pH 5.5 and 0.2 M sodium chloride. The M^{pro}−rupintrivir cocrystals were grown at room temperature by the hanging drop vapor diffusion method in a 24-well VDX hanging drop tray (Hampton Research). The $P2_1$ crystals grew at 22% (w/v) PEG 3350 with a protease concentration of 6.0 mg/mL with a 6-fold molar excess of rupintrivir (10% dimethyl sulfoxide (DMSO)). The $P2_12_12$ crystals grew at 19% (w/v) PEG 3350 with a protease concentration of 12.0 mg/mL with a 3-fold molar excess of rupintrivir (10% DMSO). Both conditions were mixed with the precipitant solution at a 1:1 ratio (1 μL:1 μL) and microseeded (1:1−1:4 dilution) with a cat whisker. Crystals appeared overnight and grew to diffraction quality within a week. The $P2_12_12$ crystals had a needle-like morphology. As data were collected at 100 K, cryogenic conditions consisted of the precipitant solution supplemented with 25% glycerol.

Data Collection and Structure Determination. EV68 $3C^{pro}$−rupintrivir cocrystals and SARS-CoV-2 M^{pro}−rupintrivir cocrystals in the $P2_12_12$ space group were flash-frozen in liquid nitrogen, and diffraction data were collected at the National Synchrotron Light Source II at the Brookhaven National Laboratory, Beamline 17-ID-1 (AMX). The diffraction intensities from the synchrotron data were indexed, integrated, and scaled using energy-dispersive X-ray spectrum (XDS).[23] The M^{pro}−rupintrivir cocrystals in the $P2_1$ space group were flash-frozen under a cryostream when mounting the crystal at our in-house Rigaku_Saturn944 X-ray system, and these diffraction intensities were indexed, integrated, and scaled using HKL3000.[24] The structures were solved using molecular replacement with PHASER[25] using either an M^{pro} monomer (PDB: 7L0D)[22] or an EV68-$3C^{pro}$ monomer (PDB: 3ZV8).[26] Model building and refinement were performed using Coot[27] and Phenix.[28] During refinement, all crystals utilized optimized stereochemical weights. The EV68-$3C^{pro}$ structure required a merohedral twin law (h,-h-k,-l) during refinement. The rupintrivir ligand was designed in Maestro, and the output sdf file was used in the Phenix program eLBOW[29] to generate the cif file containing atomic positions and constraints necessary for ligand refinement. Iterative rounds of crystallographic refinement were carried out until convergence was achieved. To limit bias throughout the refinement process, 5% of the data were reserved for the free *R*-value calculation.[30] Modeling of rupintrivir and catalytic histidines were further validated with omit maps with and without simulated annealing. MolProbity[31] was applied to evaluate the final structures before deposition in the PDB.[32,33] Structure analysis, superposition, and figure generation was done using PyMOL. X-ray data collection and crystallographic refinement statistics are presented in the Supporting Information (Table S2).

■ ASSOCIATED CONTENT

Supporting Information

The Supporting Information is available free of charge at https://pubs.acs.org/doi/10.1021/acs.biochem.1c00414.

Electron density map around the inhibitor (Figure S1), comparison of $3C^{pro}$ and M^{pro} active sites (Figure S2), catalytic histidine in $3C^{pro}$ crystal structures (Figure S3); and X-ray data collection and crystallographic refinement statistics (Table S1) (PDF)

Accession Codes

The structures described here have been deposited as PDB entries 7L8H, 7L8I, and 7L8J.

■ AUTHOR INFORMATION

Corresponding Author

Celia A. Schiffer − *Department of Biochemistry and Molecular Pharmacology, University of Massachusetts Medical School, Worcester, Massachusetts 01605, United States;* orcid.org/0000-0003-2270-6613; Email: Celia.Schiffer@umassmed.edu

Authors

Gordon J. Lockbaum − *Department of Biochemistry and Molecular Pharmacology, University of Massachusetts Medical School, Worcester, Massachusetts 01605, United States;* orcid.org/0000-0003-2720-6984

Mina Henes − *Department of Biochemistry and Molecular Pharmacology, University of Massachusetts Medical School, Worcester, Massachusetts 01605, United States*

Jeong Min Lee − *Department of Biochemistry and Molecular Pharmacology, University of Massachusetts Medical School, Worcester, Massachusetts 01605, United States*

Jennifer Timm − *Department of Biochemistry and Molecular Pharmacology, University of Massachusetts Medical School, Worcester, Massachusetts 01605, United States;* orcid.org/0000-0001-9750-3293

Ellen A. Nalivaika − *Department of Biochemistry and Molecular Pharmacology, University of Massachusetts Medical School, Worcester, Massachusetts 01605, United States*

Paul R. Thompson − *Department of Biochemistry and Molecular Pharmacology, University of Massachusetts Medical School, Worcester, Massachusetts 01605, United States;* orcid.org/0000-0002-1621-3372

Nese Kurt Yilmaz − *Department of Biochemistry and Molecular Pharmacology, University of Massachusetts Medical School, Worcester, Massachusetts 01605, United States;* orcid.org/0000-0002-5036-676X

https://doi.org/10.1021/acs.biochem.1c00414
Biochemistry XXXX, XXX, XXX−XXX

Complete contact information is available at:
https://pubs.acs.org/10.1021/acs.biochem.1c00414

Notes

The authors declare no competing financial interest.

■ ACKNOWLEDGMENTS

This research was funded by National Institute of General Medical Sciences (grant numbers: R01 GM135919 and R35 GM118112) and National Institute of Allergy and Infectious Diseases (grant number: R21 AI149716). This research used beamline 17-ID-1 (AMX) of the National Synchrotron Light Source II, a U.S. Department of Energy (DOE) Office of Science User Facility operated for the DOE Office of Science by Brookhaven National Laboratory under Contract No. DE-SC0012704. The Center for BioMolecular Structure (CBMS) is primarily supported by the National Institutes of Health, National Institute of General Medical Sciences (NIGMS) through a Center Core P30 Grant (P30GM133893), and the DOE Office of Biological and Environmental Research (KP1605010).

■ REFERENCES

(1) Woolhouse, M.; Scott, F.; Hudson, Z.; Howey, R.; Chase-Topping, M. Human viruses: discovery and emergence. *Philos. Trans. R. Soc. London, Ser. B* **2012**, *367*, 2864−2871.

(2) Park, S. W.; Pons-Salort, M.; Messacar, K.; Cook, C.; Meyers, L.; Farrar, J.; Grenfell, B. T. Epidemiological dynamics of enterovirus D68 in the United States and implications for acute flaccid myelitis. *Sci. Transl. Med.* **2021**, *13*, No. eabd2400.

(3) Lamarre, D.; Anderson, P. C.; Bailey, M.; Beaulieu, P.; Bolger, G.; Bonneau, P.; Bos, M.; Cameron, D. R.; Cartier, M.; Cordingley, M. G.; Faucher, A. M.; Goudreau, N.; Kawai, S. H.; Kukolj, G.; Lagace, L.; LaPlante, S. R.; Narjes, H.; Poupart, M. A.; Rancourt, J.; Sentjens, R. E., St.; George, R.; Simoneau, B.; Steinmann, G.; Thibeault, D.; Tsantrizos, Y. S.; Weldon, S. M.; Yong, C. L.; Llinas-Brunet, M. An NS3 protease inhibitor with antiviral effects in humans infected with hepatitis C virus. *Nature* **2003**, *426*, 186−189.

(4) Surleraux, D. L.; Tahri, A.; Verschueren, W. G.; Pille, G. M.; de Kock, H. A.; Jonckers, T. H.; Peeters, A.; De Meyer, S.; Azijn, H.; Pauwels, R.; de Bethune, M. P.; King, N. M.; Prabu-Jeyabalan, M.; Schiffer, C. A.; Wigerinck, P. B. Discovery and selection of TMC114, a next generation HIV-1 protease inhibitor. *J. Med. Chem.* **2005**, *48*, 1813−1822.

(5) El Bouzidi, K.; White, E.; Mbisa, J. L.; Sabin, C. A.; Phillips, A. N.; Mackie, N.; Pozniak, A. L.; Tostevin, A.; Pillay, D.; Dunn, D. T. HIV-1 drug resistance mutations emerging on darunavir therapy in PI-naive and-experienced patients in the UK. *J. Antimicrob. Chemother.* **2016**, *71*, 3487−3494.

(6) De Meyer, S.; Azijn, H.; Surleraux, D.; Jochmans, D.; Tahri, A.; Pauwels, R.; Wigerinck, P.; de Béthune, M.-P. TMC114, a novel human immunodeficiency virus type 1 protease inhibitor active against protease inhibitor-resistant viruses, including a broad range of clinical isolates. *Antimicrob. Agents Chemother.* **2005**, *49*, 2314−2321.

(7) Mengist, H. M.; Dilnessa, T.; Jin, T. Structural Basis of Potential Inhibitors Targeting SARS-CoV-2 Main Protease. *Front. Chem.* **2021**, *9*, No. 622898.

(8) Ghahremanpour, M. M.; Tirado-Rives, J.; Deshmukh, M.; Ippolito, J. A.; Zhang, C. H.; Cabeza de Vaca, I.; Liosi, M. E.; Anderson, K. S.; Jorgensen, W. L. Identification of 14 Known Drugs as Inhibitors of the Main Protease of SARS-CoV-2. *ACS Med. Chem. Lett.* **2020**, *11*, 2526−2533.

(9) Bafna, K.; White, K.; Harish, B.; Rosales, R.; Ramelot, T. A.; Acton, T. B.; Moreno, E.; Kehrer, T.; Miorin, L.; Royer, C. A.; Garcia-Sastre, A.; Krug, R. M.; Montelione, G. T. Hepatitis C virus drugs that inhibit SARS-CoV-2 papain-like protease synergize with remdesivir to suppress viral replication in cell culture. *Cell Rep.* **2021**, *35*, No. 109133.

(10) Matthews, D. A.; Dragovich, P. S.; Webber, S. E.; Fuhrman, S. A.; Patick, A. K.; Zalman, L. S.; Hendrickson, T. F.; Love, R. A.; Prins, T. J.; Marakovits, J. T.; Zhou, R.; Tikhe, J.; Ford, C. E.; Meador, J. W.; Ferre, R. A.; Brown, E. L.; Binford, S. L.; Brothers, M. A.; DeLisle, D. M.; Worland, S. T. Structure-assisted design of mechanism-based irreversible inhibitors of human rhinovirus 3C protease with potent antiviral activity against multiple rhinovirus serotypes. *Proc. Natl. Acad. Sci. U.S.A.* **1999**, *96*, 11000−11007.

(11) Binford, S. L.; Maldonado, F.; Brothers, M. A.; Weady, P. T.; Zalman, L. S.; Meador, J. W., 3rd; Matthews, D. A.; Patick, A. K. Conservation of amino acids in human rhinovirus 3C protease correlates with broad-spectrum antiviral activity of rupintrivir, a novel human rhinovirus 3C protease inhibitor. *Antimicrob. Agents Chemother.* **2005**, *49*, 619−626.

(12) Hayden, F. G.; Turner, R. B.; Gwaltney, J. M.; Chi-Burris, K.; Gersten, M.; Hsyu, P.; Patick, A. K.; Smith, G. J., 3rd; Zalman, L. S. Phase II, randomized, double-blind, placebo-controlled studies of ruprintrivir nasal spray 2-percent suspension for prevention and treatment of experimentally induced rhinovirus colds in healthy volunteers. *Antimicrob. Agents Chemother.* **2003**, *47*, 3907−3916.

(13) Hsyu, P. H.; Pithavala, Y. K.; Gersten, M.; Penning, C. A.; Kerr, B. M. Pharmacokinetics and safety of an antirhinoviral agent, ruprintrivir, in healthy volunteers. *Antimicrob. Agents Chemother.* **2002**, *46*, 392−397.

(14) Zhang, X.-N.; Song, Z. G.; Jiang, T.; Shi, B. S.; Hu, Y. W.; Yuan, Z. H. Rupintrivir is a promising candidate for treating severe cases of Enterovirus-71 infection. *World J. Gastroenterol.* **2010**, *16*, 201−209.

(15) Sun, L.; Meijer, A.; Froeyen, M.; Zhang, L.; Thibaut, H. J.; Baggen, J.; George, S.; Vernachio, J.; van Kuppeveld, F. J.; Leyssen, P.; Hilgenfeld, R.; Neyts, J.; Delang, L. Antiviral Activity of Broad-Spectrum and Enterovirus-Specific Inhibitors against Clinical Isolates of Enterovirus D68. *Antimicrob. Agents Chemother.* **2015**, *59*, 7782−7785.

(16) Shie, J. J.; Fang, J. M.; Kuo, T. H.; Kuo, C. J.; Liang, P. H.; Huang, H. J.; Wu, Y. T.; Jan, J. T.; Cheng, Y. S.; Wong, C. H. Inhibition of the severe acute respiratory syndrome 3CL protease by peptidomimetic alpha,beta-unsaturated esters. *Bioorg. Med. Chem.* **2005**, *13*, 5240−5252.

(17) Vatansever, E. C.; Yang, K.; Kratch, K. C.; Drelich, A.; Cho, C. C.; Mellott, D. M.; Xu, S.; Tseng, C. K.; Liu, W. R., Targeting the SARS-CoV-2 Main Protease to Repurpose Drugs for COVID-19. *BioRxiv* **2020**.

(18) Wang, J.; Fan, T.; Yao, X.; Wu, Z.; Guo, L.; Lei, X.; Wang, J.; Wang, M.; Jin, Q.; Cui, S. Crystal structures of enterovirus 71 3C protease complexed with rupintrivir reveal the roles of catalytically important residues. *J. Virol.* **2011**, *85*, 10021−10030.

(19) Ullrich, S.; Nitsche, C. The SARS-CoV-2 main protease as drug target. *Bioorg. Med. Chem. Lett.* **2020**, *30*, No. 127377.

(20) Fabrega-Ferrer, M.; Perez-Saavedra, J.; Herrera-Morande, A.; Coll, M. 7P35 Structure of the SARS-CoV-2 3CL protease in complex with rupintrivir. July 21, 2021 ed.; RCSB PDB, 2021.

(21) Verma, N.; Henderson, J. A.; Shen, J. Proton-Coupled Conformational Activation of SARS Coronavirus Main Proteases and Opportunity for Designing Small-Molecule Broad-Spectrum Targeted Covalent Inhibitors. *J. Am. Chem. Soc.* **2020**, *142*, 21883−21890.

(22) Lockbaum, G. J.; Reyes, A. C.; Lee, J. M.; Tilvawala, R.; Nalivaika, E. A.; Ali, A.; Kurt Yilmaz, N.; Thompson, P. R.; Schiffer, C. A. Crystal Structure of SARS-CoV-2 Main Protease in Complex with the Non-Covalent Inhibitor ML188. *Viruses* **2021**, *13*, 174.

(23) Kabsch, W. Xds. *Acta Crystallogr., Sect. D: Biol. Crystallogr.* **2010**, *66*, 125−132.

(24) Otwinowski, Z.; Minor, W. [20] Processing of X-ray diffraction data collected in oscillation mode. In *Methods in Enzymology*; Elsevier, 1997; Vol. *276*, pp 307−326.

(25) McCoy, A. J.; Grosse-Kunstleve, R. W.; Adams, P. D.; Winn, M. D.; Storoni, L. C.; Read, R. J. Phaser crystallographic software. *J. Appl. Crystallogr.* **2007**, *40*, 658−674.
(26) Tan, J.; George, S.; Kusov, Y.; Perbandt, M.; Anemuller, S.; Mesters, J. R.; Norder, H.; Coutard, B.; Lacroix, C.; Leyssen, P.; Neyts, J.; Hilgenfeld, R. 3C protease of enterovirus 68: structure-based design of Michael acceptor inhibitors and their broad-spectrum antiviral effects against picornaviruses. *J. Virol.* **2013**, *87*, 4339−4351.
(27) Emsley, P.; Cowtan, K. Coot: model-building tools for molecular graphics. *Acta Crystallogr., Sect. D: Biol. Crystallogr.* **2004**, *60*, 2126−2132.
(28) Adams, P. D.; Afonine, P. V.; Bunkoczi, G.; Chen, V. B.; Davis, I. W.; Echols, N.; Headd, J. J.; Hung, L. W.; Kapral, G. J.; Grosse-Kunstleve, R. W.; McCoy, A. J.; Moriarty, N. W.; Oeffner, R.; Read, R. J.; Richardson, D. C.; Richardson, J. S.; Terwilliger, T. C.; Zwart, P. H. PHENIX: a comprehensive Python-based system for macromolecular structure solution. *Acta Crystallogr., Sect. D: Biol. Crystallogr.* **2010**, *66*, 213−221.
(29) Moriarty, N. W.; Grosse-Kunstleve, R. W.; Adams, P. D. electronic Ligand Builder and Optimization Workbench (eLBOW): a tool for ligand coordinate and restraint generation. *Acta Crystallogr., Sect. D: Biol. Crystallogr.* **2009**, *65*, 1074−1080.
(30) Brünger, A. T. Free R value: a novel statistical quantity for assessing the accuracy of crystal structures. *Nature* **1992**, *355*, 472−475.
(31) Davis, I. W.; Leaver-Fay, A.; Chen, V. B.; Block, J. N.; Kapral, G. J.; Wang, X.; Murray, L. W.; Arendall, W. B., 3rd; Snoeyink, J.; Richardson, J. S.; Richardson, D. C. MolProbity: all-atom contacts and structure validation for proteins and nucleic acids. *Nucleic Acids Res.* **2007**, *35*, W375−W383.
(32) Berman, H. M.; Westbrook, J.; Feng, Z.; Gilliland, G.; Bhat, T. N.; Weissig, H.; Shindyalov, I. N.; Bourne, P. E. The Protein Data Bank. *Nucleic Acids Res.* **2000**, *28*, 235−242.
(33) Berman, H.; Henrick, K.; Nakamura, H. Announcing the worldwide Protein Data Bank. *Nat. Struct. Mol. Biol.* **2003**, *10*, 980.

https://doi.org/10.1021/acs.biochem.1c00414
Biochemistry XXXX, XXX, XXX−XXX